

$\mathcal{O}(\alpha_s)$ QCD and $\mathcal{O}(\alpha_{ew})$ electroweak corrections to $t\bar{t}h^0$ production in $\gamma\gamma$ collision *

Chen Hui², Ma Wen-Gan^{1,2}, Zhang Ren-You², Zhou Pei-Jun²,
Hou Hong-Sheng² and Sun Yan-Bin²

¹ CCAST (World Laboratory), P.O.Box 8730, Beijing 100080, P.R.China

² Department of Modern Physics, University of Science and Technology
of China (USTC), Hefei, Anhui 230027, P.R.China

Abstract

We calculate the $\mathcal{O}(\alpha_s)$ QCD and $\mathcal{O}(\alpha_{ew})$ electroweak one-loop corrections in the Standard Model framework, to the production of an intermediate Higgs boson associated with $t\bar{t}$ pair via $\gamma\gamma$ fusion at an electron-positron linear collider (LC). We find the $\mathcal{O}(\alpha_s)$ QCD corrections can be larger than the $\mathcal{O}(\alpha_{ew})$ electroweak ones, with the variations of the Higgs boson mass m_h and e^+e^- colliding energy \sqrt{s} . Both corrections may significantly decrease or increase the Born cross section. The numerical results show that the relative corrections from QCD to the process $e^+e^- \rightarrow \gamma\gamma \rightarrow t\bar{t}h^0$ may reach 34.8%, when $\sqrt{s} = 800$ GeV and $m_h = 200$ GeV, while those from electroweak can be -13.1% , -15.8% and -12.0% , at $\sqrt{s} = 800$ GeV, 1 TeV and 2 TeV respectively.

PACS: 14.65.Ha, 14.80.Bn, 12.15.Lk, 12.38.Bx

Keywords: Associated Higgs boson production, QCD correction, electroweak correction, photon collider

*Supported by National Natural Science Foundation of China.

I Introduction

After the discovery of top quark, directly searching for Higgs boson and studying its property are the main goals of the high energy colliders. In the electroweak minimal standard model(MSM), Higgs mechanism generates electroweak symmetry breaking and the Yukawa coupling terms between Higgs boson and fermions in the Lagrangian [1, 2]. In the SM, the Yukawa term reads $\mathcal{L}_Y = -\sum_f m_f (1 + H(x)/v) \bar{\psi}_f \psi_f$. There the coupling strength of the fermion-Higgs Yukawa coupling $f - \bar{f} - h^0$ is predicted as $g_{f\bar{f}h} = m_f/v$ at the tree level, where $v = (\sqrt{2}G_F)^{-1/2} \simeq 246$ GeV is the vacuum expectation value of the Higgs field. Since the top quark is the heaviest fermion, the top quark Yukawa coupling $g_{t\bar{t}h}$ should be the strongest one among all the fermion-Higgs couplings, e.g., $g_{t\bar{t}h}^2 \simeq 0.5$ to be compared for example with $g_{b\bar{b}h}^2 \simeq 4 \times 10^{-4}$. Therefore, the Higgs boson production associated with a top-quark pair production process is particularly important in collider physics for probing the top-quark Yukawa coupling with the intermediate mass of Higgs boson.

Recently, LEP2 experiments have provided a lower bound of 114.4 GeV for the SM Higgs boson mass at the 95% confidence level[3]. The future linear colliders (LC) will continue the work in searching for Higgs boson and studying its property. There have been already some detailed designs of linear colliders, such as NLC[4], JLC[5], TESLA[6] and CLIC[7]. Although the cross section for $e^+e^- \rightarrow t\bar{t}h^0$ process is small at a LC, about 1 fb for $\sqrt{s} = 500$ GeV and $m_h = 100$ GeV [8, 9, 10], it has a distinctive experimental signature and can potentially be used to measure the top-quark Yukawa coupling with intermediate Higgs mass at a LC with very high luminosity.

As we know the apparently the clean signal for light Higgs boson production associated with a

top quark pair is $e^+e^- \rightarrow t\bar{t}h^0 \rightarrow b\bar{b}b\bar{b}W^+W^-$ in both semileptonic and fully hadronic decay channels. This leads to multi-jet event topologies involving at least 6 or more jets in the final state, with ≥ 4 b-jets and multi-jet invariant mass constraints. Obviously, its measurement has many difficulties, for example, the tiny signal with backgrounds about 3 orders of magnitude larger, the limitations of jet-clustering algorithm in properly reconstructing multi-jets in the final state, and the degradation of b-tagging performance due to hard gluon radiation and jet mixing. The potential backgrounds are from the $t\bar{t}Z^0$ and $t\bar{t}$ productions. The dominant electroweak background is:

$$\gamma\gamma \rightarrow t\bar{t}Z^0 \rightarrow b\bar{b}W^+W^-Z^0 \rightarrow b\bar{b}b\bar{b}l^\pm\nu q\bar{q}'. \quad (1.1)$$

The largest background is from radiative top quark decay:

$$\gamma\gamma \rightarrow t\bar{t} \rightarrow b\bar{b}W^+W^-g \rightarrow b\bar{b}b\bar{b}l^\pm\nu q\bar{q}'. \quad (1.2)$$

Since the b-jets resulting from the gluon splitting are logarithmically enhanced at low energy, cuts on the jet energy are efficient at eliminating this background[11]. The weak corrections to $\gamma\gamma \rightarrow t\bar{t}h^0$ should involve the real emissions of W and Z^0 gauge bosons. These may be other sources of electroweak backgrounds. Our calculation shows that the cross section of the real emission of Z^0 gauge boson in $t\bar{t}h^0$ production via $\gamma\gamma$ collision is under 0.1% of the $\gamma\gamma \rightarrow t\bar{t}h^0$ process, and can be neglected in our analysis, while for the real W emission $t\bar{t}h^0$ production the cross section is in the same order as that of the $\gamma\gamma \rightarrow t\bar{t}h^0$ process. In principle, these backgrounds can easily be removed by using the constraints due to the W , Z^0 , t and h^0 masses with perfect b-tagging and reconstruction of multi-jets. However, this may not be true in practice. The experimental situation of the signal detection of $t\bar{t}h^0$ production will be even worse, considering the following two fields. Firstly, the detectors have a finite coverage in

polar angle. Some of these real W bosons can be emitted so close to the beam direction that part of their decay products may well escape detection. Secondly, all three particles in the $t\bar{t}h^0$ final state are highly unstable, and would decay in the detector. If $m_h \gtrsim 130 \text{ GeV}$, it would mostly produce $b\bar{b}$ pairs. If above, it would yield four fermions, either leptons/neutrinos or quarks, principally via $h^0 \rightarrow WW^*$ decays. Besides, top quark(anti-quark) decays into three objects, a b -quark and the decay products of the W , leptons/neutrinos or quarks. Hence, at tree level in these decays, we are looking at 8- or 10-fermion final states. In the most likely case in which the fermions arising from the W decays are quarks, additional (mainly gluon) radiation will take place, so that at detector level more than 10 jets may be extracted. Therefore, the additional real W radiation and $t\bar{t}Z^0$ production entering the detector region could be uneasy to resolved through their decay products in the data samples of $t\bar{t}h^0$ events.

Expected experimental accuracy for determination of the $t\bar{t}h^0$ coupling in $e^+e^- \rightarrow t\bar{t}h^0$ process has been discussed in many literatures for specialized linear collider. They show that the experimental accuracy depends very much on the b-tagging efficiency. For example, the top quark Yukawa coupling can be measured to 6–8% accuracy with integral luminosity 1000 fb^{-1} at an e^+e^- linear collider with $\sqrt{s} = 1 \text{ TeV}$, assuming 100% efficiency for b-jet tagging and including statistic but not systematic errors. The accuracy of the measurement drops to 17–22% if only a 60% efficiency for b-tagging is achieved [11, 12]. The references [13, 14, 15] also stated that the precise determination of the top-Higgs coupling via the measurement of $e^+e^- \rightarrow t\bar{t}h^0$ process can reach the accuracy of few percent. Therefore, if we assume the machine and detector are very efficient and the background processes can be distinguished substantially, the evaluation of radiative corrections could be significant for the

accurate experimental measurements of $e^+e^- \rightarrow t\bar{t}h^0$ process. In Ref.[9], S. Dawson and L. Reina presented the NLO QCD corrections to process $e^+e^- \rightarrow t\bar{t}h^0$. And in references [16, 17, 18] the electroweak corrections to the process $e^+e^- \rightarrow t\bar{t}h^0$ are calculated. The supersymmetric electroweak corrections to process $e^+e^- \rightarrow t\bar{t}h^0$ were already discussed by X.H. Wu, et al[19].

An e^+e^- LC can also be designed to operate as a $\gamma\gamma$ collider. This is achieved by using Compton backscattered photons in the scattering of intense laser photons on the initial e^+e^- beams. The resulting $\gamma - \gamma$ center of mass system (CMS) energy is peaked at about $0.8\sqrt{s}$ for the appropriate choices of machine parameters. In $\gamma\gamma$ collision mode at the high energy peak, we may get approximately the same luminosity as that of e^+e^- collision. With the new possibility of $\gamma\gamma$ collisions at electron-positron linear colliders, the production process $e^+e^- \rightarrow \gamma\gamma \rightarrow t\bar{t}h^0$ offers another approach to probe directly the top-Higgs coupling in addition to $e^+e^- \rightarrow t\bar{t}h^0$ and $pp(p\bar{p}) \rightarrow t\bar{t}h^0$ processes. To detect the Higgs boson associated with a top-quark pair in high colliding energy, $\gamma\gamma$ collision has an outstanding advantage over e^+e^- collision due to its relative larger production rate. The reason is that at the tree level the $e^+e^- \rightarrow t\bar{t}h^0$ process has a ‘s-channel suppression’ from the virtual photon and Z^0 propagators, especially for the heavy masses of the final particles. Therefore, we can conclude that the $e^+e^- \rightarrow \gamma\gamma \rightarrow t\bar{t}h^0$ process provides a better approach than e^+e^- collision to produce $t\bar{t}h^0$. Similar with the measurement of the process $e^+e^- \rightarrow t\bar{t}h^0$, the evaluation of radiative corrections for process $\gamma\gamma \rightarrow t\bar{t}h^0$ is also significant for the accurate experimental measurements of top quark Yukawa coupling.

The Born cross section of $e^+e^- \rightarrow \gamma\gamma \rightarrow t\bar{t}h^0$ process was calculated already in previous work of Ref.[20]. In this paper we neglect the real gauge boson radiation effects and present the calculations

of the $\mathcal{O}(\alpha_s)$ QCD and $\mathcal{O}(\alpha_{ew})$ electroweak corrections to $e^+e^- \rightarrow \gamma\gamma \rightarrow t\bar{t}h^0$ in the SM. We draw a comparison between our numerical results of Born cross sections of $\gamma\gamma \rightarrow t\bar{t}h^0$ and those in Ref.[20]. The paper is organized as follow. In section 2, we present the notations and analytical calculations of the QCD and the electroweak radiative corrections. The numerical results and discussions are presented in section 3. Our conclusions are given in section 4. The numerical comparison of the Born cross section of process $e^+e^- \rightarrow \gamma\gamma \rightarrow t\bar{t}h^0$ are presented in Appendix.

II Analytical Calculation

II.1 Calculations of the lowest order of the $\gamma\gamma \rightarrow t\bar{t}h^0$ subprocess

The subprocess $\gamma\gamma \rightarrow t\bar{t}h^0$ at the lowest level occurs through the u- and t-channel mechanisms involving Higgs boson bremsstrahlungs originated from different positions on top-quark lines. The tree level diagrams are drawn in Fig.1, but the corresponding diagrams with interchange of the two incoming photons are not shown.

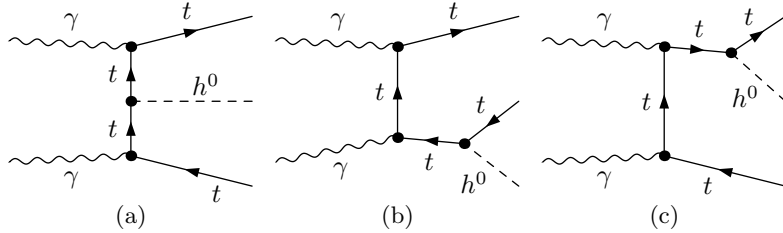


Figure 1: The lowest order diagrams for the $\gamma\gamma \rightarrow t\bar{t}h^0$ subprocess.

We denote the subprocess $\gamma\gamma \rightarrow t\bar{t}h^0$ as

$$\gamma(p_1) + \gamma(p_2) \rightarrow t(k_1) + \bar{t}(k_2) + h^0(k_3). \quad (2.1)$$

The four-momenta of incoming electron and positron are denoted as p_1 and p_2 , respectively, and the

four-momenta of outgoing top-quark, anti-top-quark and Higgs boson are represented as k_1 , k_2 and k_3 correspondingly. All these momenta obey the on-shell equations $p_1^2 = p_2^2 = 0$, $k_1^2 = k_2^2 = m_t^2$ and $k_3^2 = m_h^2$.

The amplitudes of the corresponding t-channel Feynman diagrams (shown in Fig.1(a-c)) of the subprocess $\gamma\gamma \rightarrow t\bar{t}h^0$ are represented by

$$\begin{aligned} \mathcal{M}_t^{(a)} = & -\frac{e^3 Q_t^2 m_t}{2m_W \sin \theta_W} \frac{1}{(k_1 - p_1)^2 - m_t^2} \frac{1}{(p_2 - k_2)^2 - m_t^2} \\ & \times \bar{u}(k_1) \not{e}(p_1) (\not{k}_1 - \not{p}_1 + m_t) (\not{p}_2 - \not{k}_2 + m_t) \not{e}(p_2) v(k_2), \end{aligned} \quad (2.2)$$

$$\begin{aligned} \mathcal{M}_t^{(b)} = & -\frac{e^3 Q_t^2 m_t}{2m_W \sin \theta_W} \frac{1}{(k_1 - p_1)^2 - m_t^2} \frac{1}{(k_2 + k_3)^2 - m_t^2} \\ & \times \bar{u}(k_1) \not{e}(p_1) (\not{k}_1 - \not{p}_1 + m_t) \not{e}(p_2) (-\not{k}_2 - \not{k}_3 + m_t) v(k_2), \end{aligned} \quad (2.3)$$

$$\begin{aligned} \mathcal{M}_t^{(c)} = & -\frac{e^3 Q_t^2 m_t}{2m_W \sin \theta_W} \frac{1}{(k_1 + k_3)^2 - m_t^2} \frac{1}{(p_2 - q_2)^2 - m_t^2} \\ & \times \bar{u}(k_1) (\not{k}_1 + \not{k}_3 + m_t) \not{e}(p_1) (\not{p}_2 - \not{k}_2 + m_t) \not{e}(p_2) v(k_2), \end{aligned} \quad (2.4)$$

where $Q_t = 2/3$ and the corresponding amplitudes of the u-channel Feynman diagrams of the subprocess $\gamma\gamma \rightarrow t\bar{t}h^0$ can be obtained by the following interchanges.

$$\mathcal{M}_u^{(a)} = \mathcal{M}_t^{(a)}(p_1 \leftrightarrow p_2), \quad \mathcal{M}_u^{(b)} = \mathcal{M}_t^{(b)}(p_1 \leftrightarrow p_2), \quad \mathcal{M}_u^{(c)} = \mathcal{M}_t^{(c)}(p_1 \leftrightarrow p_2). \quad (2.5)$$

The total amplitude at the lowest order is the summation of the above amplitudes.

$$\mathcal{M}_0 = \sum_{i=a,b}^c \sum_{j=u}^t \mathcal{M}_j^{(i)}. \quad (2.6)$$

Although the previous calculations for the $\gamma\gamma \rightarrow t\bar{t}h^0$ subprocess and $e^+e^- \rightarrow \gamma\gamma \rightarrow t\bar{t}h^0$ process at the lowest order were presented by Kingman Cheung[20], we made the numerical comparison with his

results yet. We calculated the Born cross section of the process $\gamma\gamma \rightarrow t\bar{t}h^0$ by using Feynman gauge and unitary gauge to check the gauge invariance, and adopting FeynArts 3[21] and CompHEP[22] packages respectively. We found our results are in good agreement with each other, but not coincident with Cheung's. The numerical comparisons are presented in Appendix Table 3.

II.2 Calculations of the $\mathcal{O}(\alpha_s)$ QCD corrections of the $\gamma\gamma \rightarrow t\bar{t}h^0$ subprocess

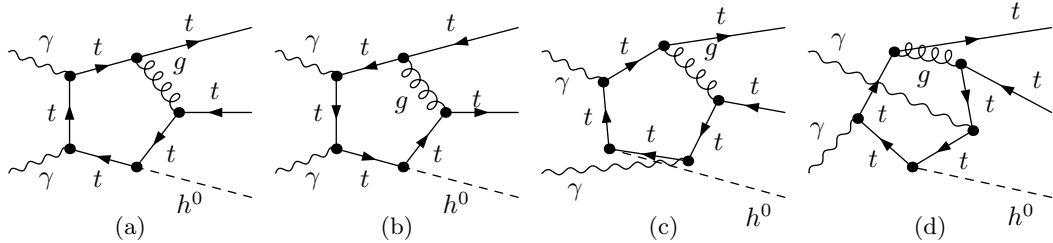


Figure 2: The QCD pentagon diagrams for the $\gamma\gamma \rightarrow t\bar{t}h^0$ subprocess, whose amplitudes include five-point tensor integrals of rank 4. The corresponding diagrams with interchange of the two incoming photons are not shown.

The $\mathcal{O}(\alpha_s)$ QCD one-loop Feynman diagrams of the subprocess $\gamma\gamma \rightarrow t\bar{t}h^0$ are generated by *FeynArts 3* [21]. There are 84 Feynman diagrams with $\mathcal{O}(\alpha_s)$ corrections of the virtual one-loop QCD corrections, which involves the vertex correction, internal propagator self-energy correction, box and pentagon diagrams. The Feynman graphs which generate amplitudes including five-point integrals of rank 4 are shown in Fig.2 as a representative selection. The amplitude of the subprocess $\gamma\gamma \rightarrow t\bar{t}h^0$ including virtual QCD corrections to $\mathcal{O}(\alpha_s)$ can be expressed as

$$\mathcal{M}_{QCD} = \mathcal{M}_0 + \frac{\alpha_s}{4\pi} C_F \mathcal{M}_{QCD}^{vir}. \quad (2.7)$$

where $C_F = 4/3$, The term $\frac{\alpha_s}{4\pi} C_F \mathcal{M}_{QCD}^{vir}$ is the amplitude contributed by the QCD one-loop Feynman

diagrams and the QCD renormalizations of top-quark wave function, mass and $t - \bar{t} - h^0$ Yukawa coupling. We define the relevant renormalization constants as

$$m_{t,0} = m_t + \delta m_{t(g)}, \quad t_0^L = (1 + \frac{1}{2} \delta Z_{t(g)}^L) t^L, \quad t_0^R = (1 + \frac{1}{2} \delta Z_{t(g)}^R) t^R, \quad g_{ttH}^0 = \frac{m_t}{v} + \frac{\delta m_{t(g)}}{v}. \quad (2.8)$$

With the on-mass-shell renormalized condition we get the $\mathcal{O}(\alpha_s)$ QCD contributed parts of the renormalization constants as

$$\delta m_{t(g)} = \frac{m_t}{2} \tilde{Re} \left(\Sigma_{t(g)}^L(m_t^2) + \Sigma_{t(g)}^R(m_t^2) + 2\Sigma_{t(g)}^S(m_t^2) \right), \quad (2.9)$$

$$\delta Z_{t(g)}^L = -\tilde{Re} \Sigma_{t(g)}^L(m_t^2) - m_t^2 \frac{\partial}{\partial p^2} \tilde{Re} \left[\Sigma_{t(g)}^L(p^2) + \Sigma_{t(g)}^R(p^2) + 2\Sigma_{t(g)}^S(p^2) \right] \Big|_{p^2=m_t^2}, \quad (2.10)$$

$$\delta Z_{t(g)}^R = -\tilde{Re} \Sigma_{t(g)}^R(m_t^2) - m_t^2 \frac{\partial}{\partial p^2} \tilde{Re} \left[\Sigma_{t(g)}^L(p^2) + \Sigma_{t(g)}^R(p^2) + 2\Sigma_{t(g)}^S(p^2) \right] \Big|_{p^2=m_t^2}, \quad (2.11)$$

\tilde{Re} takes the real part of the loop integrals appearing in the self energies only. Here we define the renormalized top-quark irreducible two-point function as

$$\hat{\Gamma}_t(p^2) = i[\not{p} P_L \hat{\Sigma}_t^L(p^2) + \not{p} P_R \hat{\Sigma}_t^R(p^2) + m_t \hat{\Sigma}_t^S(p^2)] \delta_{\alpha\beta} \quad (2.12)$$

where α and β are the color indices of the top quarks on the two sides of the self-energy diagram, $P_{L,R} = (1 \mp \gamma_5)/2$. The unrenormalized top-quark self energy parts contributed by $\mathcal{O}(\alpha_s)$ QCD read

$$\Sigma_{t(g)}^L(p^2) = \Sigma_{t(g)}^R(p^2) = \frac{g_s^2}{6\pi^2} (-1 + 2B_0[p, 0, m_t] + 2B_1[p, 0, m_t]) \quad (2.13)$$

and

$$\Sigma_{t(g)}^S(p^2) = \frac{g_s^2}{3\pi^2} (1 - 2B_0[p, 0, m_t]) \quad (2.14)$$

The corresponding contribution part to the cross section at $\mathcal{O}(\alpha_s)$ order can be written as

$$\Delta\hat{\sigma}_{vir}^{QCD} = \hat{\sigma}_0\hat{\delta}_{vir}^{QCD} = \frac{\alpha_s C_F}{8\pi|\vec{p}_1|\sqrt{\hat{s}}}\int d\Phi_3 \overline{\sum_{\text{spin}} \text{Re} \left(\mathcal{M}_0^\dagger \mathcal{M}_{QCD}^{vir} \right)}, \quad (2.15)$$

where $d\Phi_3$ is the three-body phase space element. The bar over summation recalls averaging over initial spins.

The virtual QCD corrections contain both ultraviolet (UV) and infrared (IR) divergences in general. To regularize the UV divergences in loop integrals, we adopt the dimensional regularization in which the dimensions of spinor and spacetime manifolds are extended to $D = 4 - 2\epsilon$. We have verified the cancellation of the UV both analytically and numerically. Then we get a UV finite amplitude including $\mathcal{O}(\alpha_s)$ virtual radiative corrections.

The IR divergence in the \mathcal{M}_{QCD}^{vir} of the process $\gamma\gamma \rightarrow t\bar{t}h^0$ is originated from virtual gluon corrections. It can be exactly cancelled by including the real gluon bremsstrahlung corrections to this subprocess in the soft gluon limit. The real gluon emission process is denoted as

$$\gamma(p_1) + \gamma(p_2) \rightarrow t(k_1) + \bar{t}(k_2) + h^0(k_3) + g(k), \quad (2.16)$$

where the real gluon radiates from the internal or external top(anti-top) quark line, and can be classified into two parts which behave soft and hard natures respectively. In order to isolate the soft gluon emission singularity in the real gluon emission process, we adopt the general phase-space-slicing method [33], in which the bremsstrahlung phase space is divided into singular and non-singular regions.

The cross section of the real gluon emission process (2.16) is decomposed into soft and hard terms

$$\Delta\hat{\sigma}_{real}^{QCD} = \Delta\hat{\sigma}_{soft}^{QCD} + \Delta\hat{\sigma}_{hard}^{QCD} = \hat{\sigma}_0(\hat{\delta}_{soft}^{QCD} + \hat{\delta}_{hard}^{QCD}). \quad (2.17)$$

We adopt the soft gluon approximation method with a cut ΔE in numerical calculations for the soft emission corrections ($k^0 < \Delta E$). With this approach the real gluon radiation from internal color lines does not lead to IR singularities and can be neglected in this approach. We find the contribution of the soft gluon emission process is [32, 34]

$$d\Delta\hat{\sigma}_{\text{soft}}^{QCD} = -d\hat{\sigma}_0 \frac{\alpha_s C_F}{2\pi^2} \int_{|\vec{k}| \leq \Delta E} \frac{d^3 k}{2k^0} \left[\frac{k_1}{k_1 \cdot k} - \frac{k_2}{k_2 \cdot k} \right]^2, \quad (2.18)$$

in which ΔE is the energy cutoff of the soft gluon and $k^0 \leq \Delta E \ll \sqrt{s}$. $k^0 = \sqrt{|\vec{k}|^2 + m_g^2}$ is the gluon energy. Here we have introduced a small gluon mass m_g to regulate the infrared divergences occurring in the soft emission. The integral over the soft gluon phase space have been implemented, the analytical result of the soft gluon corrections to $\gamma\gamma \rightarrow t\bar{t}h^0g$ is presented as[9]

$$\begin{aligned} \left(\frac{d\Delta\hat{\sigma}_{\text{soft}}^{QCD}}{dx_h} \right) &= \left(\frac{d\hat{\sigma}_0}{dx_h} \right) \frac{\alpha_s C_F}{2\pi} \left\{ -2 \log \left(\frac{4\Delta E^2}{m_g^2} \right) \left[1 - \frac{xk_1 \cdot k_2}{m_t^2(x^2 - 1)} \log(x^2) \right] - \frac{k_1^0}{|\vec{k}_1|} \log \left(\frac{k_1^0 - |\vec{k}_1|}{k_1^0 + |\vec{k}_1|} \right) \right. \\ &\quad - \frac{k_2^0}{|\vec{k}_2|} \log \left(\frac{k_2^0 - |\vec{k}_2|}{k_2^0 + |\vec{k}_2|} \right) + \frac{4xk_1 \cdot k_2}{m_t^2(x^2 - 1)} \left[\frac{1}{4} \log^2 \left(\frac{u^0 - |\vec{u}|}{u^0 + |\vec{u}|} \right) + \text{Li}_2 \left(1 - \frac{u^0 + |\vec{u}|}{v} \right) \right. \\ &\quad \left. \left. + \text{Li}_2 \left(1 - \frac{u^0 - |\vec{u}|}{v} \right) \right]_{u=xk_2}^{u=xk_1} \right\}, \end{aligned}$$

where

$$v = \frac{m_t^2(x^2 - 1)}{2(xk_1^0 - k_2^0)}, \quad (2.19)$$

and x is the solution of

$$m_t^2(x^2 + 1) - 2xk_1 \cdot k_2 = 0, \quad (2.20)$$

which should satisfy the constraint of

$$\frac{xk_1^0 - k_2^0}{k_2^0} > 0. \quad (2.21)$$

We checked numerically the cancellation of IR divergencies and verified that the contribution of these soft gluon bremsstrahlung corrections leads to an IR finite cross section which is independent of the infinitesimal gluon mass m_g . The hard gluon emission cross section $\Delta\hat{\sigma}_{\text{hard}}^{QCD}$ for $E_g > \Delta E$, is calculated numerically by using Monte Carlo method. The statistic error is controlled under 0.3%.

Finally the UV and IR finite total cross section of the subprocess $\gamma\gamma \rightarrow t\bar{t}h^0$ including the $\mathcal{O}(\alpha_s)$ QCD corrections reads

$$\hat{\sigma}^{QCD} = \hat{\sigma}_0 + \Delta\hat{\sigma}^{QCD} = \hat{\sigma}_0 + \Delta\hat{\sigma}_{\text{vir}}^{QCD} + \Delta\hat{\sigma}_{\text{real}}^{QCD} = \hat{\sigma}_0(1 + \hat{\delta}^{QCD}), \quad (2.22)$$

where $\hat{\delta}^{QCD} = \hat{\delta}_{\text{vir}}^{QCD} + \hat{\delta}_{\text{soft}}^{QCD} + \hat{\delta}_{\text{hard}}^{QCD}$ is the QCD relative correction of order $\mathcal{O}(\alpha_s)$.

II.3 The calculation of the $\mathcal{O}(\alpha_{\text{ew}})$ one-loop corrections to the $\gamma\gamma \rightarrow t\bar{t}h^0$ subprocess

In addition to the QCD corrections, we also calculate the $\mathcal{O}(\alpha_{\text{ew}})$ one-loop electroweak corrections to the subprocess $\gamma\gamma \rightarrow t\bar{t}h^0$. We use again the package *FeynArts 3*[21] to generate the electroweak one-loop Feynman diagrams and the relevant amplitudes of the subprocess $\gamma\gamma \rightarrow t\bar{t}h^0$ automatically. The electroweak one-loop Feynman diagrams can be classified into self-energy, triangle, box and pentagon diagrams. The pentagon diagrams, whose corresponding amplitudes include five-point tensor integrals of rank 4, are depicted in Fig.3 as a representative selection. In our electroweak correction calculation we use also the t'Hooft-Feynman gauge and adopt the definitions of one-loop integral functions of Ref.[29]. The one-loop level virtual electroweak corrections to $\gamma\gamma \rightarrow t\bar{t}h^0$ can be expressed as

$$\Delta\hat{\sigma}_{\text{vir}}^{EW} = \hat{\sigma}_0\hat{\delta}_{\text{vir}}^{EW} = \frac{N_c}{2|\vec{p}_1|\sqrt{\hat{s}}}\int d\Phi_3 \sum_{\text{spin}} \text{Re} \left(\mathcal{M}_0^\dagger \mathcal{M}_{\text{vir}}^{EW} \right), \quad (2.23)$$

where \vec{p}_1 is the c.m.s. three-momentum of one of the incoming photons, $d\Phi_3$ is the three-body phase space element, and the bar over summation recalls averaging over initial spins. $\mathcal{M}_{\text{vir}}^{EW}$ is the amplitude of the electroweak one-loop Feynman diagrams, including self-energy, vertex, box, pentagon and counterterm diagrams.

Analogously to the case of the QCD correction calculations shown in last subsection, we adopt the dimensional regularization scheme to regularize the UV divergences in loop integrals. We assume that there is no quark mixing, the KM-matrix is identity matrix and use the complete on-mass-shell (COMS) renormalization scheme [32], in which the electric charge of electron e and the physical masses m_W , m_Z , m_h , m_t et al., are chosen to be the renormalized parameters. The relevant field renormalization constants are defined as [32]

$$\begin{aligned} e_0 &= (1 + \delta Z_e)e, & m_{h,0}^2 &= m_h^2 + \delta m_h^2, & m_{t,0} &= m_t + \delta m_t, & m_{W,0}^2 &= m_W^2 + \delta m_W^2, \\ m_{Z,0}^2 &= m_Z^2 + \delta m_Z^2, & A_0 &= \frac{1}{2}\delta Z_{AZ}Z + (1 + \frac{1}{2}\delta Z_{AA})A, & h_0 &= (1 + \frac{1}{2}\delta Z_h)h, \\ t_0^L &= (1 + \frac{1}{2}\delta Z^L)t^L, & t_0^R &= (1 + \frac{1}{2}\delta Z^R)t^R. \end{aligned} \quad (2.24)$$

With the on-mass-shell conditions, we can obtain the renormalized constants expressed as

$$\begin{aligned} \delta m_W^2 &= \tilde{R}e\Sigma_T^W(m_W^2), & \delta m_Z^2 &= Re\Sigma_T^{ZZ}(m_Z^2), & \delta Z_{AA} &= -\frac{\partial\Sigma_T^{AA}(p^2)}{\partial p^2}|_{p^2=0}, \\ \delta Z_{ZZ} &= -Re\frac{\partial\Sigma_T^{ZZ}(p^2)}{\partial p^2}|_{p^2=m_Z^2}, & \delta Z_{ZA} &= 2\frac{\Sigma_T^{ZA}(0)}{m_Z^2}, & \delta Z_{AZ} &= -2Re\frac{\Sigma_T^{AZ}(m_Z^2)}{m_Z^2}, \\ \delta m_h &= Re\Sigma^h(m_h^2), & \delta Z_h &= -Re\frac{\partial\Sigma^h(p^2)}{\partial p^2}|_{p^2=m_h^2}. \end{aligned} \quad (2.25)$$

The renormalization constants of the wave function and mass of top-quark can be evaluated from Eqs.(2.9)-(2.11) upon replacing the QCD top-quark self-energies($\Sigma_{t(g)}^L$, $\Sigma_{t(g)}^R$ and $\Sigma_{t(g)}^S$) by the elec-

trweak corresponding ones (Σ_t^L , Σ_t^R and Σ_t^S), respectively. And the explicit expressions of the electroweak self energies in the SM concerned in our calculations can be found in the Appendix B of Ref.[32]. The UV divergence appearing from the one-loop diagrams is cancelled by the contributions of the counterterm diagrams in our calculations. We have verified both analytically and numerically that the final cross sections including $\mathcal{O}(\alpha_{ew})$ virtual radiative corrections and the corresponding counterterm contributions are UV finite. The further verification of the correctness for the one-loop calculation is made by probing the gauge independence of cross section via changing the value of ξ in R_ξ gauge, and the results are coincident with each other very well.

Analogous to the calculation of the QCD corrections, the IR divergence in the subprocess $\gamma\gamma \rightarrow t\bar{t}h^0$ originates from virtual photonic corrections is cancelled by the real photonic bremsstrahlung corrections in the soft photon limit. We use also the general phase-space-slicing method [33] and divide the phase space into singular and non-singular regions. Then the cross section of the real photon emission subprocess ($\gamma\gamma \rightarrow t\bar{t}h^0\gamma$) is decomposed into soft and hard parts.

$$\Delta\hat{\sigma}_{\text{real}} = \Delta\hat{\sigma}_{\text{soft}} + \Delta\hat{\sigma}_{\text{hard}} = \hat{\sigma}_0(\hat{\delta}_{\text{soft}}^\gamma + \hat{\delta}_{\text{hard}}^\gamma). \quad (2.26)$$

By using the soft photon ($k^0 < \Delta E$) approximation, we get the contribution of the soft photon emission subprocess expressed as [32, 34]

$$d\Delta\hat{\sigma}_{\text{soft}}^\gamma = -d\hat{\sigma}_0 \frac{\alpha_{ew} Q_t^2}{2\pi^2} \int_{|\vec{k}| \leq \Delta E} \frac{d^3 k}{2k_0} \left[\frac{k_1}{k_1 \cdot k} - \frac{k_2}{k_2 \cdot k} \right]^2, \quad (2.27)$$

in which ΔE is the energy cutoff of the soft photon and $k^0 \leq \Delta E \ll \sqrt{\hat{s}}$, $Q_t = 2/3$ is the electric charges of top quark, $k^0 = \sqrt{|\vec{k}|^2 + m_\gamma^2}$ is the photon energy. Therefore, after the integration over the soft photon phase space, we obtain the analytical result of the soft corrections to $\gamma\gamma \rightarrow t\bar{t}h^0$. Actually,

the real photonic emission correction can be deduced from the real gluon emission corrections upon replacing the factor $C_F\alpha_s$ by $Q^2\alpha_{ew}$. The cancellation of IR divergencies is verified and the results of the cross section show the independence on the infinitesimal photon mass m_γ in our calculation.

Since sometimes the QED radiative contributions can be quite large, the investigation of the genuine weak corrections quantitatively would help us to understand the origination of the large electroweak corrections. The QED correction to the subprocess $\gamma\gamma \rightarrow t\bar{t}h^0$ is gauge invariant and comprises three parts: (1) photonic virtual radiations of final and internal top-quarks, (2) real photonic radiations from final and internal top-quarks, (3) the interference of final and internal real photon radiations. Actually, the total $\mathcal{O}(\alpha_{ew})$ order QED corrections for the subprocess $\gamma\gamma \rightarrow t\bar{t}h^0$, can be obtained numerically from the results of the $\mathcal{O}(\alpha_s)$ order QCD corrections as presented in section II.2 through multiplying a factor of $\frac{\alpha_{ew}Q_t^2}{\alpha_s(\mu)C_F}$. Then the genuine weak corrections can be evaluated by subtracting the QED corrections from the $\mathcal{O}(\alpha_{ew})$ QED corrections. We define the genuine weak relative correction as,

$$\hat{\delta}_w = \hat{\delta} - \hat{\delta}^{QED} = \hat{\delta} - \hat{\delta}_{vir}^{QED} - \hat{\delta}_{soft}^{QED} - \hat{\delta}_{hard}^{QED}. \quad (2.28)$$

where $\hat{\delta}_{vir}^{QED}$ is the relative correction contributed by the QED one-loop diagrams including virtual photon exchange and the corresponding parts of the counter terms. $\hat{\delta}_{soft}^{QED}$ and $\hat{\delta}_{hard}^{QED}$ are the relative corrections of the soft and hard real photon emissions, respectively.

II.4 Calculations of process $e^+e^- \rightarrow \gamma\gamma \rightarrow t\bar{t}h^0$

By using the laser back-scattering technique on electron beam, an e^+e^- LC which has c.m.s. energy of hundred GeV to several TeV can be transformed to be a photon collider [24, 25, 26]. By integrating

over the photon luminosity in an e^+e^- linear collider, the total cross section of the process $e^+e^- \rightarrow \gamma\gamma \rightarrow t\bar{t}h^0$ can be obtained in the form as

$$\sigma(s) = \int_{E_0/\sqrt{s}}^{x_{max}} dz \frac{d\mathcal{L}_{\gamma\gamma}}{dz} \hat{\sigma}(\gamma\gamma \rightarrow t\bar{t}h \text{ at } \hat{s} = z^2 s) \quad (2.29)$$

where $E_0 = 2m_t + m_h$, and $\sqrt{s}(\sqrt{\hat{s}})$ being the $e^+e^- (\gamma\gamma)$ c.m.s. energy. $\frac{d\mathcal{L}_{\gamma\gamma}}{dz}$ is the distribution function of photon luminosity, which is defined as:

$$\frac{d\mathcal{L}_{\gamma\gamma}}{dz} = 2z \int_{z^2/x_{max}}^{x_{max}} \frac{dx}{x} F_{\gamma/e}(x) F_{\gamma/e}(z^2/x) \quad (2.30)$$

For the initial unpolarized electrons and laser photon beams, the energy spectrum of the back scattered photon is given by [27]

$$F_{\gamma/e} = \frac{1}{D(\xi)} \left[1 - x + \frac{1}{1-x} - \frac{4x}{\xi(1-x)} + \frac{4x^2}{\xi^2(1-x)^2} \right] \quad (2.31)$$

where $x = 2\omega/\sqrt{s}$ is the fraction of the energy of the incident electron carried by the back-scattered photon, the maximum fraction of energy carried by the back-scattered photon is $x_{max} = 2\omega_{max}/\sqrt{s} = \xi/(1+\xi)$, and

$$D(\xi) = \left(1 - \frac{4}{\xi} - \frac{8}{\xi^2} \right) \ln(1+\xi) + \frac{1}{2} + \frac{8}{\xi} - \frac{1}{2(1+\xi)^2}, \quad (2.32)$$

$$\xi = \frac{2\sqrt{s}\omega_0}{m_e^2}. \quad (2.33)$$

m_e and $\sqrt{s}/2$ are the mass and energy of the electron, ω_0 is the laser-photon energy. In our evaluation, we choose ω_0 such that it maximizes the backscattered photon energy without spoiling the luminosity through e^+e^- pair creation. Then we have $\xi = 2(1 + \sqrt{2})$, $x_{max} \simeq 0.83$, and $D(\xi) \approx 1.84$, as used in Ref.[28].

III Numerical results and discussions

For the numerical calculation we use the following input parameters [35]

$$\begin{aligned}
\alpha_{\text{ew}}(0)^{-1} &= 137.03599976, & m_W &= 80.423 \text{ GeV}, & m_Z &= 91.1876 \text{ GeV}, \\
m_e &= 0.510998902 \text{ MeV}, & m_\mu &= 105.658357 \text{ MeV}, & m_\tau &= 1.77699 \text{ GeV}, \\
m_u &= 66 \text{ MeV}, & m_c &= 1.2 \text{ GeV}, & m_t &= 174.3 \text{ GeV}, \\
m_d &= 66 \text{ MeV}, & m_s &= 150 \text{ MeV}, & m_b &= 4.3 \text{ GeV}, \\
\alpha_s(m_Z^2) &= 0.117186.
\end{aligned}$$

where we use the effective values of the light quark masses (m_u and m_d) which can reproduce the hadron contribution to the shift in the fine structure constant $\alpha_{\text{ew}}(m_Z^2)$ [36], and take the pole mass of top quark($m_t = 174.3 \text{ GeV}$) to determine the $t\bar{t}h^0$ coupling strength. The QCD renormalization scale μ is taken to be $(2m_t + m_h)/2$ and the running of the strong coupling $\alpha_s(\mu^2)$ is evaluated at the two-loop level(\overline{MS} scheme) with five active flavors.

The numerical results of the cross sections with QCD and one-loop electroweak radiative corrections for the subprocess $\gamma\gamma \rightarrow t\bar{t}h^0$ are plotted in Fig.4 and Fig.5, respectively. The full, dashed, and dash-dotted curves correspond to the cases with $m_h = 115, 150$ and 200 GeV , correspondingly, and $\gamma\gamma$ colliding energy $\sqrt{\hat{s}}$ runs from the value little larger than the threshold $(2m_t + m_h)$ to 1.8 TeV . For each line type there are two curves, the upper curve (in the region $\sqrt{\hat{s}} > 1 \text{ TeV}$) is for the Born cross section and the lower one for the QCD corrected cross section. As indicated in Fig.4, the QCD corrections can increase (when $\sqrt{\hat{s}} < 650 \text{ GeV}$) or decrease the cross sections of subprocess $\gamma\gamma \rightarrow t\bar{t}h^0$ (when $\sqrt{\hat{s}} > 900 \text{ GeV}$), while Fig.5 shows that the one-loop electroweak radiative corrections always reduce the Born cross sections in the plotted energy range of $\sqrt{\hat{s}}$. The curves in both Fig.4 and Fig.5 show that all the Born, QCD and electroweak corrected cross sections decrease with the increment of

the mass of Higgs boson m_h . The curves for $m_h = 115$ GeV increase rapidly to their corresponding maximal cross section values, when the $\gamma\gamma$ colliding energy $\sqrt{\hat{s}}$ goes from the threshold value to the corresponding position of peak. The curves for $m_h = 150$ GeV have platforms when $\sqrt{\hat{s}}$ are larger than 1000 GeV, and for $m_h = 200$ GeV both Born and one-loop corrected cross sections increase slowly in the whole plotted range of $\sqrt{\hat{s}}$.

We define the QCD relative corrections to the subprocess $\gamma\gamma \rightarrow t\bar{t}h^0$ and parent process $e^+e^- \rightarrow \gamma\gamma \rightarrow t\bar{t}h^0$ as

$$\hat{\delta}^{QCD} = \frac{\hat{\sigma}^{QCD} - \hat{\sigma}_0}{\hat{\sigma}_0}, \quad \delta^{QCD} = \frac{\sigma^{QCD} - \sigma_0}{\sigma_0}, \quad (3.1)$$

respectively, and the electroweak relative corrections to the subprocess $\gamma\gamma \rightarrow t\bar{t}h^0$ and process $e^+e^- \rightarrow \gamma\gamma \rightarrow t\bar{t}h^0$ as

$$\hat{\delta} = \frac{\hat{\sigma} - \hat{\sigma}_0}{\hat{\sigma}_0}, \quad \delta = \frac{\sigma - \sigma_0}{\sigma_0}, \quad (3.2)$$

correspondingly. The $\mathcal{O}(\alpha_s)$ QCD relative corrections and $\mathcal{O}(\alpha_{ew})$ electroweak relative corrections to the cross sections for $\gamma\gamma \rightarrow t\bar{t}h^0$ subprocess, corresponding to Fig.4 and Fig.5, are depicted in Fig.6 and Fig.7(a-b), respectively. We can read from Fig.6 that the QCD relative corrections to the subprocess $\gamma\gamma \rightarrow t\bar{t}h^0$ decrease from 111% to -13.8% when the c.m.s. energy $\sqrt{\hat{s}}$ increases from the threshold energy to 1.8 TeV. From Fig.7(a) we can see that in the plotted colliding energy range, the $\mathcal{O}(\alpha_{ew})$ order electroweak relative corrections to subprocess $\gamma\gamma \rightarrow t\bar{t}h^0$ can reach -7.98% and -16.5% for $m_h = 115$ GeV and 200 GeV, respectively. The maximal electroweak absolute relative corrections to the cross sections $|\hat{\delta}|_{max}$ and the corresponding $\sqrt{\hat{s}}$ positions for subprocess $\gamma\gamma \rightarrow t\bar{t}h^0$

with $m_h = 115, 130, 150, 170, 200$ GeV are listed in Table 1. In Fig.7(b) the $\mathcal{O}(\alpha_{ew})$ order QED and genuine weak relative corrections are depicted, respectively. It shows that the $\mathcal{O}(\alpha_{ew})$ QED relative corrections are very small comparing with the genuine weak relative corrections, and can only reach 1.28% for the curve of $m_h = 200$ GeV at the position of $\sqrt{\hat{s}} \sim 580$ GeV.

We also depicted the QCD and electroweak relative corrections to the cross sections of subprocess $\gamma\gamma \rightarrow t\bar{t}h^0$ as the functions of the mass of Higgs boson m_h with $\sqrt{\hat{s}} = 500, 800, 1000, 2000$ GeV in Fig.8 and Fig.9, respectively. Both curves for $\sqrt{\hat{s}} = 500$ GeV in Fig.8 and Fig.9 are truncated before the position of $m_h \sim 150$ GeV, because the channel $\gamma\gamma \rightarrow t\bar{t}h^0$ cannot be opened when $\sqrt{\hat{s}} < m_h + 2m_t$. On the curves for $\sqrt{\hat{s}} = 800, 1000, 2000$ GeV in Fig.9, there exist two resonance peaks on each curve at the positions $m_h \sim 2m_Z$ and $m_h \sim 2m_W$. Since we didn't consider the widths of W^\pm and Z^0 gauge bosons in loop calculation, the genuine one-loop weak corrections in the vicinities of the thresholds at $m_h = 2m_W$ and $m_h = 2m_Z$ shown in Fig.9 are untrustworthy. In Fig.8, the QCD relative corrections for $\sqrt{\hat{s}} = 500$ GeV are rather large, and can reach the value larger than 110% when the $m_h = 140$ GeV and $\sqrt{\hat{s}} = 500$ GeV, while the QCD relative corrections are in the range 1.74% \sim -14.0%, when $\sqrt{\hat{s}} = 800, 1000, 2000$ GeV. Fig.9 shows that the curves of the electroweak relative corrections for $\sqrt{\hat{s}} = 800$ GeV and 1000 GeV go down from -6.48% to -16.0% and from -7.01% to -13.9% respectively, when m_h varies from 100 GeV to 200 GeV. While the electroweak relative corrections for $\sqrt{\hat{s}} = 2000$ GeV are relative stable(about minus a few percent) except in the Higgs mass regions satisfying resonance conditions.

Fig.10 and Fig.11 show the cross sections including $\mathcal{O}(\alpha_s)$ QCD and $\mathcal{O}(\alpha_{ew})$ radiative corrections and for $e^+e^- \rightarrow \gamma\gamma \rightarrow t\bar{t}h^0$ process versus the e^+e^- colliding energy \sqrt{s} , respectively. Both figures

demonstrate that the Born and radiative corrected cross sections increase with the increment of \sqrt{s} , and the $\mathcal{O}(\alpha_s)$ QCD radiative corrections for different values of m_h can reduce or increase the Born cross sections, but the $\mathcal{O}(\alpha_{ew})$ electroweak corrections reduce the Born cross section only in the plotted range of electron-positron c.m.s. energy \sqrt{s} . The QCD and electroweak relative corrections for the $e^+e^- \rightarrow \gamma\gamma \rightarrow t\bar{t}h^0$ parent process corresponding to Fig.10 and Fig.11, are depicted in Fig.12 and Fig.13, respectively. We can see that the QCD relative correction can be very large near the threshold colliding energy, while the electroweak relative corrections can reach -15.9% for $m_h = 200$ GeV in the vicinity of $\sqrt{s} \sim 1$ TeV. The maximum absolute electroweak relative corrections for different Higgs boson mass values in the plotted colliding c.m.s. energy range can be read out from this figure and are listed in Table 2.

The QCD and electroweak relative corrections to the cross section of the process $e^+e^- \rightarrow \gamma\gamma \rightarrow t\bar{t}h^0$ as the functions of the Higgs boson mass m_h are depicted in Fig.14 and Fig.15 with $\sqrt{s} = 800$, 1000, 2000 GeV, respectively. From Fig.14 we can see that the QCD one-loop relative correction for $\sqrt{s} = 800$ GeV can reach 34.8% at the position of $m_h = 200$ GeV. In Fig.15 two resonance peaks appear again on each curve at the positions of $m_h \sim 2m_Z$ and $m_h \sim 2m_W$ because of the resonance effects, and the correction values in these vicinities are untrustworthy. For the curves of $m_h = 800$ GeV and $m_h = 1000$ GeV, the relative correction decrease from -2.66% and -4.51% to -13.1% and -15.9% , respectively, when m_h varies from 100 GeV to 200 GeV. The relative correction for $\sqrt{s} = 2000$ GeV varies in the range of $[-6.15\%, -12.0\%]$ when m_h goes from 100 GeV to 200 GeV, except in the h^0 mass regions satisfying the resonance effect conditions.

Scale dependence of the K -factors ($= \frac{\sigma^{QCD}}{\sigma_0}$) of the total cross sections for the process $e^+e^- \rightarrow$

$\gamma\gamma \rightarrow t\bar{t}h^0$ at LC ($m_h = 115 \text{ GeV}$) is plotted in Fig.16. The full-line, dashed-line and dash-dotted-line correspond to $\sqrt{s} = 800 \text{ GeV}$, 1 TeV and 2 TeV , respectively. We can see from the figure that when the scale μ goes from 100 GeV to 1 TeV , the QCD K -factors vary from $1.176, 1.039, 0.900$ to $1.134, 1.029, 0.924$ for $\sqrt{s} = 800 \text{ GeV}, 1000 \text{ GeV}, 2000 \text{ GeV}$, respectively. We can conclude that the theoretical uncertainty of the QCD correction at $\mathcal{O}(\alpha_s)$ level due to the variation of energy scale μ , is under 4% for $\sqrt{s} = 800, 1000, 2000 \text{ GeV}$, when $m_h = 115 \text{ GeV}$ and energy scale μ is in the range of 100 GeV to 1 TeV .

IV Summary

In this paper we calculate the $\mathcal{O}(\alpha_s)$ QCD and $\mathcal{O}(\alpha_{\text{ew}})$ one-loop electroweak radiative corrections to the $e^+e^- \rightarrow \gamma\gamma \rightarrow t\bar{t}h^0$ process with Higgs boson in intermediate mass region at an e^+e^- linear collider (LC) in the SM. We investigate the dependence of the QCD and electroweak radiative corrections to both subprocess $\gamma\gamma \rightarrow t\bar{t}h^0$ and parent process $e^+e^- \rightarrow \gamma\gamma \rightarrow t\bar{t}h^0$ on the Higgs boson mass m_h and colliding energy $\sqrt{\hat{s}}$ (\sqrt{s}), and find that the QCD corrections can either increase or decrease the Born cross section, while the electroweak corrections always decrease the Born cross section of the $e^+e^- \rightarrow \gamma\gamma \rightarrow t\bar{t}h^0$ parent process and $\gamma\gamma \rightarrow t\bar{t}h^0$ subprocess in the Higgs boson mass range $115 \text{ GeV} < m_h < 200 \text{ GeV}$. We also notice that the $\mathcal{O}(\alpha_s)$ QCD corrections to process $e^+e^- \rightarrow \gamma\gamma \rightarrow t\bar{t}h^0$ can be larger than the $\mathcal{O}(\alpha_{\text{ew}})$ corrections depending on the Higgs boson mass m_h and e^+e^- colliding energy \sqrt{s} . Both kinds of corrections may significantly decrease or increase the Born cross sections. The numerical results show that the $\mathcal{O}(\alpha_s)$ QCD relative corrections to the process $e^+e^- \rightarrow \gamma\gamma \rightarrow t\bar{t}h^0$ can reach 34.8% when $\sqrt{s} = 800 \text{ GeV}$ and $m_h = 200 \text{ GeV}$, while the $\mathcal{O}(\alpha_{\text{ew}})$ electroweak relative

corrections to the Born cross sections can reach -13.1% , -15.8% and -12.0% at $\sqrt{s} = 800$ GeV, 1 TeV and 2 TeV, respectively.

Acknowledgments: This work was supported in part by the National Natural Science Foundation of China and a grant from the University of Science and Technology of China.

Appendix

In Appendix we list the numerical comparison of the cross sections at the tree level for the process $e^+e^- \rightarrow \gamma\gamma \rightarrow t\bar{t}h^0$. In order to check our calculation we use two independently developed packages *FeynArts 3*[21] and *CompHEP*[22] to evaluate the cross sections. The results of ours and Kingman Cheung's [20] are presented in Table 3. It is clear that our cross sections at tree level are not coincident with Cheung's results.

References

- [1] S. L. Glashow, Nucl. Phys. **22**, 579 (1961); S. Weinberg, Phys. Rev. Lett. **1**, 1264 (1967); A. Salam, Proc. 8th Nobel Symposium Stockholm 1968, ed. N. Svartholm(Almqvist and Wiksells, Stockholm 1968) p.367; H. D. Politzer, Phys. Rep. **14**, 129 (1974).
- [2] P. W. Higgs, Phys. Lett. **12**, 132 (1964); Phys. Rev. Lett. **13**, 508 (1964); Phys. Rev. **145**, 1156 (1966); F. Englert and R. Brout, Phys. Rev. Lett. **13**, 321 (1964); G. S. Guralnik, C. R. Hagen and T. W. B. Kibble, Phys. Rev. Lett. **13**, 585 (1964); T. W. B. Kibble, Phys. Rev. **155**, 1554 (1967).

- [3] ALEPH, DELPHI, L3 and OPAL Collaborations, The LEP working group for Higgs boson search, LHWG Note 2002-01 (July 2002), contributed paper for ICHEP'02 (Amsterdam, July 2002), and additional updates at <http://lephiggs.web.cern.ch/LEPHIGGS/www/Welcome.html>; P. A. McNamara and S. L. Wu, *Rept. Prog. Phys.* **65**, 465 (2002).
- [4] C. Adolphsen *et al.*, (International Study Group Collaboration), “International study group progress report on linear collider development”, SLAC-R-559 and KEK-REPORT-2000-7 (April, 2000).
- [5] N. Akasaka *et al.*, “JLC design study”, KEK-REPORT-97-1.
- [6] R. Brinkmann, K. Flottmann, J. Rossbach, P. Schmuser, N. Walker and H. Weise(editor), “TESLA: The superconducting electron positron linear collider with an integrated X-ray laser laboratory. Technical design report, Part 2: The Accelerator”, DESY-01-11 (March, 2001).
- [7] “A 3 TeV e^+e^- Linear Collider Based on CLIC Technology”, G. Guignard(editor), CERN-2000-008.
- [8] S. Dittmaier, M. Krämer, Y. Liao, M. Spira and P. M. Zerwas, *Phys. Lett.* **B441**, 383 (1998).
- [9] S. Dawson and L. Reina, *Phys. Rev.* **D59**, 054012 (1999), arXiv:hep-ph/9808443.
- [10] A. Juste and G. Merino, arXiv:hep-ph/9910301.
- [11] T. Abe et al. [American Linear Collider Working Group Collaboration], “Linear collider physics resource book for Snowmass 2001”, in Proc. of the APS/DPF/DPB Summer Study on

the Future of Particle Physics (Snowmass 2001) arXiv:hep-ex/0106055, arXiv:hep-ex/0106056, arXiv:hep-ex/0106057, arXiv:hep-ex/0106058, and the references therein.

- [12] H. Baer, S. Dawson and L. Reina, Phys. Rev. **D61** (1999) 013002. therein.
- [13] J. A. Aguilar-Saavedra et al. [ECFA/DESY LC Physics Working Group Collaboration], “TESLA Technical Design Report Part III:Physics at an e^+e^- -Linear Collider”, arXiv:hep-ph/0106315, and the references therein.
- [14] K. Abe et al., [ACFA Linear Collider Working Group Collaboration], “Particle physics experiments at JLC”, arXiv:hep-ph/0109166, and the references therein.
- [15] M. Battaglia and K. Desch, arXiv:hep-ph/0101165 and references therein.
- [16] Y. You, W.-G. Ma, H. Chen, R.-Y. Zhang, Y.-B. Sun, H.-S. Hou, Phys.Lett.B571(2003)85, arXiv:hep-ph/0306036.
- [17] G. Belanger, F. Boudjema, J. Fujimoto, T. Ishikawa, T. Kaneko, K. Kato, Y. Shimizu and Y. Yasui, Phys.Lett.B571(2003)163, arXiv:hep-ph/0307029.
- [18] A. Denner, S. Dittmaier, M. Roth, M. M. Weber, Phys.Lett.B575(2003)290, arXiv:hep-ph/0307193.
- [19] X.H. Wu, C.S. Li and J.J. Liu, arXiv:hep-ph/0308012.
- [20] Kingman Cheung, Phys. Rev. D47 (1993) 3750, arXiv:hep-ph/9211262.
- [21] T. Hahn, Comp. Phys. Commun. **140**, 418 (2001).

[22] A.Pukhov, E.Boos, et al.,“CompHEP - a package for evaluation of Feynman diagrams and integration over multi-particle phase space. User’s manual for version 33”, arXiv:hep-ph/9908288.

[23] G.P. Lepage, J. Comput. Phys. **27** (1978)192 and CLNS-80/447.

[24] I. Ginzburg, G. Kotkin, V. Serbo and V. Telnov, Pizma ZhETF, **34** (1981) 514; JETP Lett. **34** (1982) 491. Preprint INP 81-50, 1981, Novosibirsk.

[25] I. Ginzburg, G. Kotkin, V. Serbo and V. Telnov, Nucl. Instr. & Meth. **205** (1983) 47, Preprint INP 81-102, 1991, Novosibirsk.

[26] I. Ginzburg, G. Kotkin, S. Panfil, V. Serbo and V. Telnov, Nucl. Instr. & Meth. **219** (1984) 5.

[27] V. Telnov, Nucl. Instrum. Methods Phys. Res. **A294**(1990)72; L. Ginzburg, G. Kotkin and H. Spiesberger, Fortschr. Phys. **34**(1986)687.

[28] K. Cheung, Phys.Rev. **D47**(1993)3750.

[29] G. Passarino and M. Veltman, Nucl. Phys. **B160**, 151 (1979).

[30] A. Denner and S. Dittmaier, Nucl.Phys. **B658**, 175 (2003).

[31] G. ’t Hooft and M. Veltman, Nucl. Phys. **B44**, 189 (1972).

[32] A. Denner, Fortschr. Phys. **41**, 307 (1993).

[33] W. T. Giele and E. W. Glover, Phys. Rev. **D46**, 1980 (1992); W. T. Giele, E. W. Glover and D. A. Kosower, Nucl. Phys. **B403**, 633 (1993); S. Keller and E. Laenen, Phys. Rev. **D59**, 114004 (1999).

[34] G.'t Hooft and M. Veltman, Nucl. Phys. **B153**, 365 (1979).

[35] K. Hagiwara, *et al.*, Phy. Rev. **D66**, 1 (2002).

[36] F. Legerlehner, DESY 01-029, arXiv:hep-ph/0105283.

Figure Captions

Figure 1 The lowest order diagrams for the $\gamma\gamma \rightarrow t\bar{t}h^0$ subprocess..

Figure 2 The QCD pentagon diagrams for the $\gamma\gamma \rightarrow t\bar{t}h^0$ subprocess, whose amplitudes include five-point tensor integrals of rank 4. The corresponding diagrams with interchange of the two incoming photons are not shown.

Figure 3 The five-point pentagon electroweak one-loop diagrams for the $\gamma\gamma \rightarrow t\bar{t}h^0$ subprocess, whose corresponding amplitudes include five-point tensor integrals of rank 4.

Figure 4 The Born and one-loop QCD corrected cross sections for the $\gamma\gamma \rightarrow t\bar{t}h^0$ subprocess as the functions of c.m.s. energy ($\sqrt{\hat{s}}$) with $m_h = 115, 150, 200$ GeV, respectively. For each line type, the upper curve (in the energy region $\sqrt{\hat{s}} > 1$ TeV) is for the Born cross section and the lower one for the one-loop QCD corrected cross section.

Figure 5 The Born and one-loop electroweak corrected cross sections for the $\gamma\gamma \rightarrow t\bar{t}h^0$ subprocess as the functions of c.m.s. energy ($\sqrt{\hat{s}}$) with $m_h = 115, 150, 200$ GeV. For each line type, the upper curve is for the Born cross section and the lower one for the one-loop electroweak corrected cross section.

Figure 6 The QCD one-loop relative corrections as the functions of c.m.s. energy ($\sqrt{\hat{s}}$) for the $\gamma\gamma \rightarrow t\bar{t}h^0$ subprocess with $m_h = 115, 150, 200$ GeV, respectively.

Figure 7 (a)The electroweak one-loop relative corrections as the functions of c.m.s. energy ($\sqrt{\hat{s}}$) with $m_h = 115, 150, 200$ GeV for the $\gamma\gamma \rightarrow t\bar{t}h^0$ subprocess. (b)The QED and weak one-loop relative corrections as the functions of c.m.s. energy ($\sqrt{\hat{s}}$) with $m_h = 115, 150, 200$ GeV for the $\gamma\gamma \rightarrow t\bar{t}h^0$ subprocess. For each line type, the upper curve is for the QED corrected cross section and the lower one for the weak corrected cross section.

Figure 8 The QCD one-loop relative corrections as the functions of the mass of Higgs boson (m_h) for the $\gamma\gamma \rightarrow t\bar{t}h^0$ subprocess with $\sqrt{\hat{s}} = 500, 800, 1000, 2000$ GeV, respectively.

Figure 9 The electroweak one-loop relative corrections as the functions of the mass of Higgs boson (m_h) for the $\gamma\gamma \rightarrow t\bar{t}h^0$ subprocess with $\sqrt{\hat{s}} = 500, 800, 1000, 2000$ GeV, respectively.

Figure 10 The Born and one-loop QCD corrected cross sections for the $e^+e^- \rightarrow \gamma\gamma \rightarrow t\bar{t}h^0$ process as the functions of c.m.s. energy ($\sqrt{\hat{s}}$) with $m_h = 115, 150, 200$ GeV, respectively. For each line type, the upper curve(in the energy region $\sqrt{\hat{s}} > 1.4$ TeV) is for the Born cross section and the lower one presents the one-loop corrected cross section.

Figure 11 The Born and one-loop electroweak corrected cross sections for the $e^+e^- \rightarrow \gamma\gamma \rightarrow t\bar{t}h^0$ process as the functions of c.m.s. energy ($\sqrt{\hat{s}}$) with $m_h = 115, 150, 200$ GeV, respectively. For each line type, the upper curve is for the Born cross section and the lower one presents the one-loop corrected cross section.

Figure 12 The QCD one-loop relative corrections to the $e^+e^- \rightarrow \gamma\gamma \rightarrow t\bar{t}h^0$ process as the functions of c.m.s. energy ($\sqrt{\hat{s}}$) with $m_h = 115, 150, 200$ GeV, respectively.

Figure 13 The electroweak one-loop relative corrections to the $e^+e^- \rightarrow \gamma\gamma \rightarrow t\bar{t}h^0$ process as the functions of c.m.s. energy (\sqrt{s}) with $m_h = 115, 150, 200$ GeV, respectively.

Figure 14 The QCD one-loop relative corrections to the $e^+e^- \rightarrow \gamma\gamma \rightarrow t\bar{t}h^0$ process as the functions of Higgs boson mass (m_h) with $\sqrt{s} = 800, 1000, 2000$ GeV.

Figure 15 The electroweak one-loop relative corrections as the functions of Higgs boson mass (m_h) with $\sqrt{s} = 800, 1000, 2000$ GeV, respectively.

Figure 16 The QCD relative corrections to the $e^+e^- \rightarrow \gamma\gamma \rightarrow t\bar{t}h^0$ process as the function of the QCD renormalization scale μ , with $m_h = 115$ GeV and $\sqrt{s} = 800, 1000, 2000$ GeV.

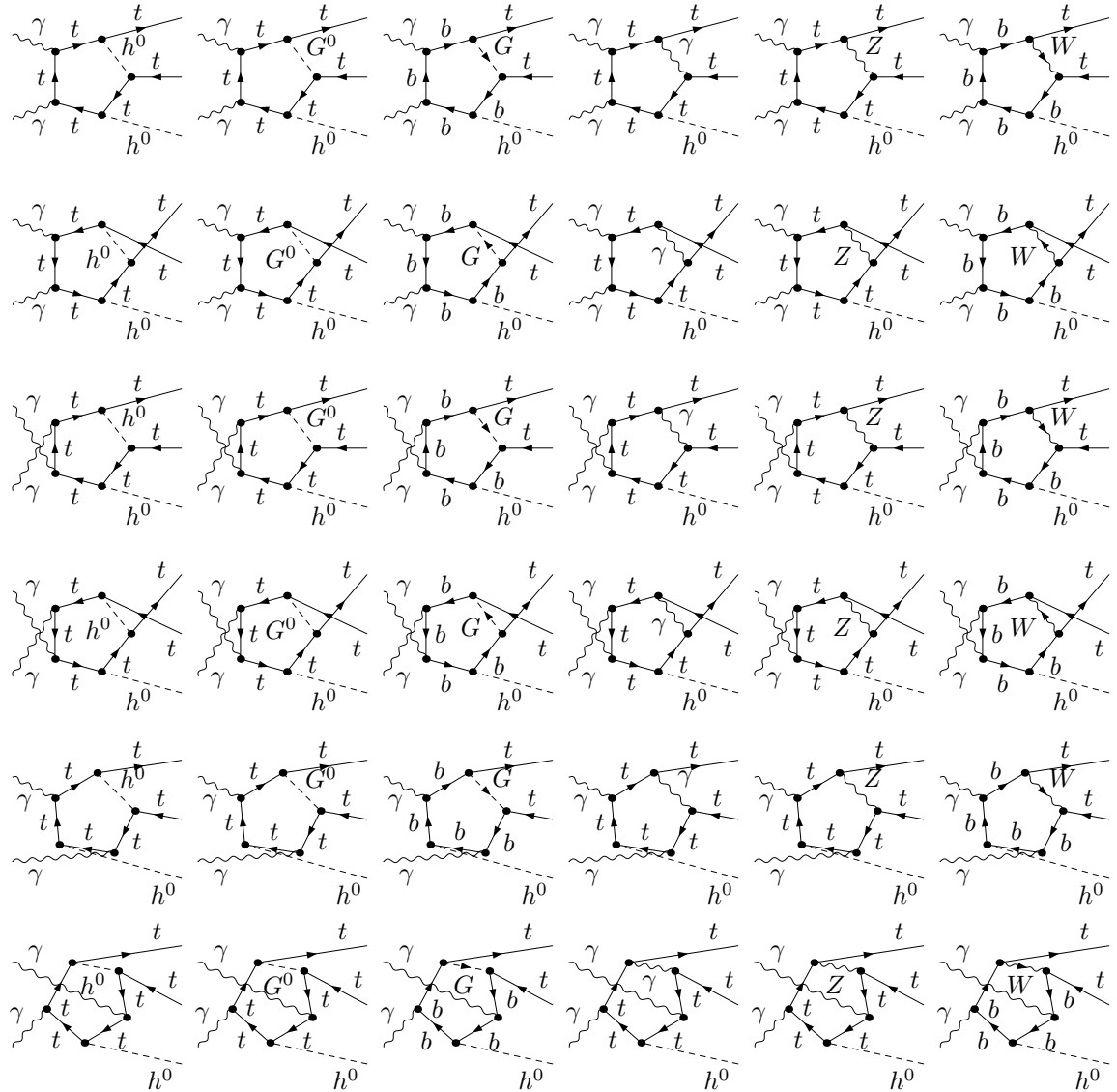


Figure 3: The five-point pentagon electroweak one-loop diagrams for the $\gamma\gamma \rightarrow t\bar{t}h^0$ subprocess, whose corresponding amplitudes include five-point tensor integrals of rank 4.

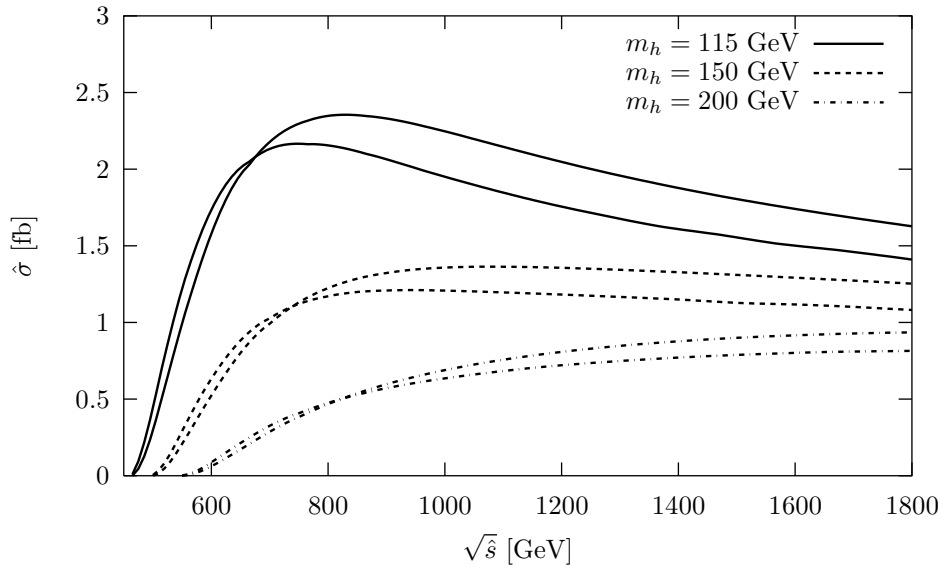


Figure 4: The Born and one-loop QCD corrected cross sections for the $\gamma\gamma \rightarrow t\bar{t}h^0$ subprocess as the functions of c.m.s. energy ($\sqrt{\hat{s}}$) with $m_h = 115, 150, 200$ GeV, respectively. For each line type, the upper curve(in the energy region $\sqrt{\hat{s}} > 1$ TeV) is for the Born cross section and the lower one for the one-loop QCD corrected cross section.

m_h (GeV)	$\sqrt{\hat{s}}$ (GeV)	$ \hat{\delta} _{max}$ (%)
115	1000	7.98
130	950	9.15
150	890	11.5
170	820	14.0
200	710	16.5

Table 1: The maximum electroweak absolute relative corrections and the corresponding colliding energy $\sqrt{\hat{s}}$ positions for the $\gamma\gamma \rightarrow t\bar{t}h^0$ subprocess with $m_h = 115, 130, 150, 170, 200$ GeV, respectively.

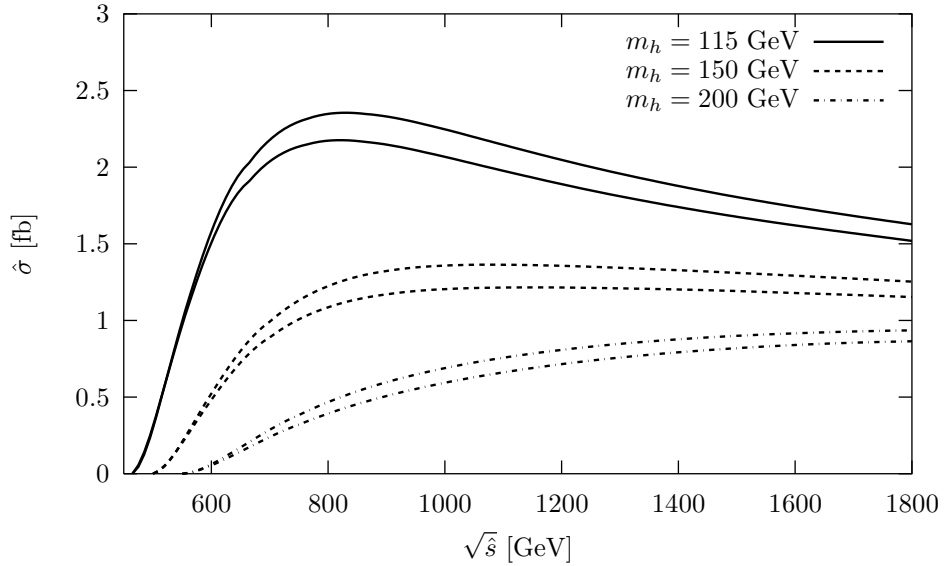


Figure 5: The Born and one-loop electroweak corrected cross sections for the $\gamma\gamma \rightarrow t\bar{t}h^0$ subprocess as the functions of c.m.s. energy ($\sqrt{\hat{s}}$) with $m_h = 115, 150, 200$ GeV. For each line type, the upper curve is for the Born cross section and the lower one for the one-loop electroweak corrected cross section.

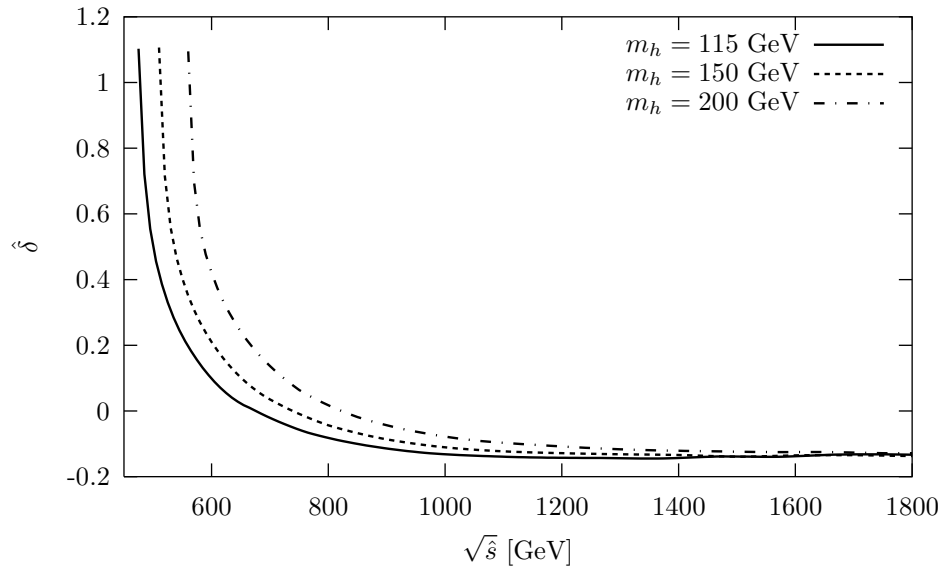


Figure 6: The QCD one-loop relative corrections as the functions of c.m.s. energy ($\sqrt{\hat{s}}$) for the $\gamma\gamma \rightarrow t\bar{t}h^0$ subprocess with $m_h = 115, 150, 200$ GeV, respectively.

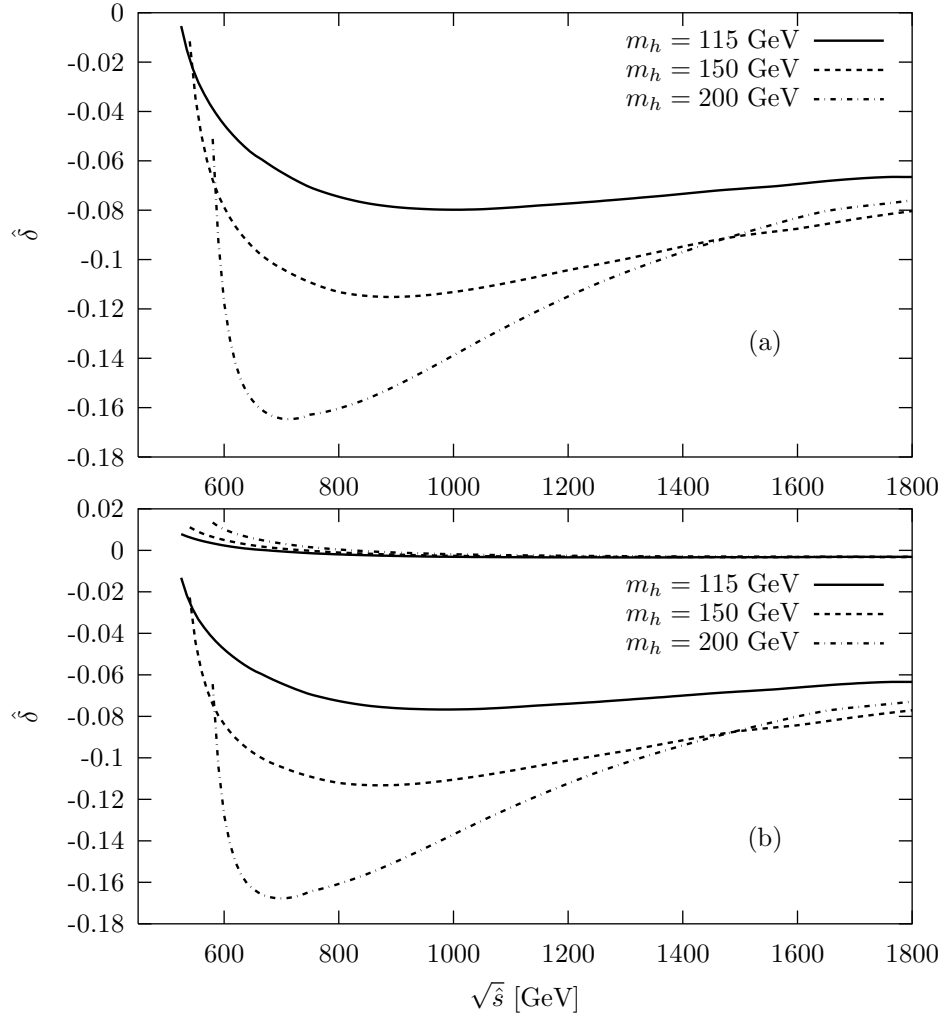


Figure 7: (a) The electroweak one-loop relative corrections as the functions of c.m.s. energy ($\sqrt{\hat{s}}$) with $m_h = 115, 150, 200$ GeV for the $\gamma\gamma \rightarrow t\bar{t}h^0$ subprocess. (b) The QED and weak one-loop relative corrections as the functions of c.m.s. energy ($\sqrt{\hat{s}}$) with $m_h = 115, 150, 200$ GeV for the $\gamma\gamma \rightarrow t\bar{t}h^0$ subprocess. For each line type, the upper curve is for the QED corrected cross section and the lower one for the weak corrected cross section.

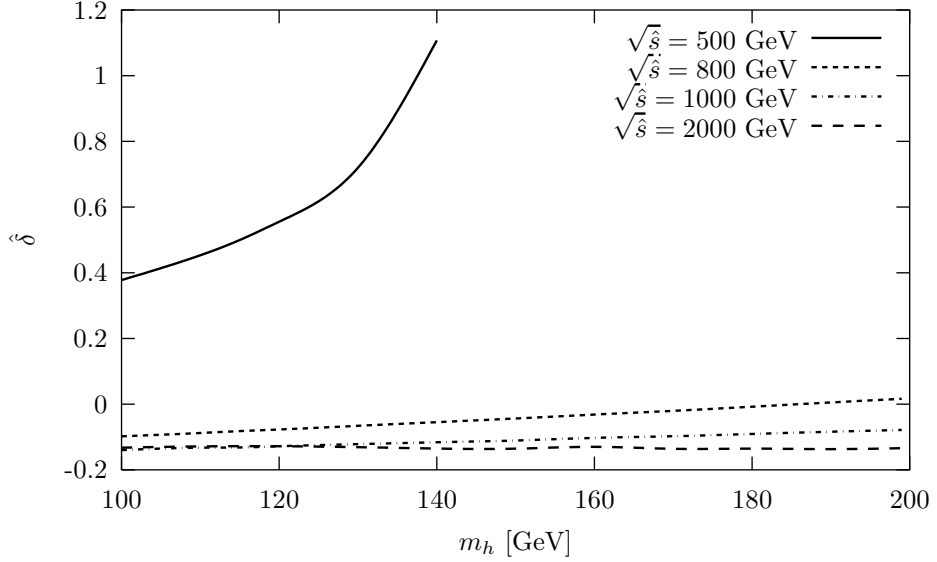


Figure 8: The QCD relative corrections to the cross sections of $\gamma\gamma \rightarrow t\bar{t}h^0$ subprocess as the functions of the mass of Higgs boson (m_h) with $\sqrt{\hat{s}} = 500, 800, 1000, 2000$ GeV, respectively.

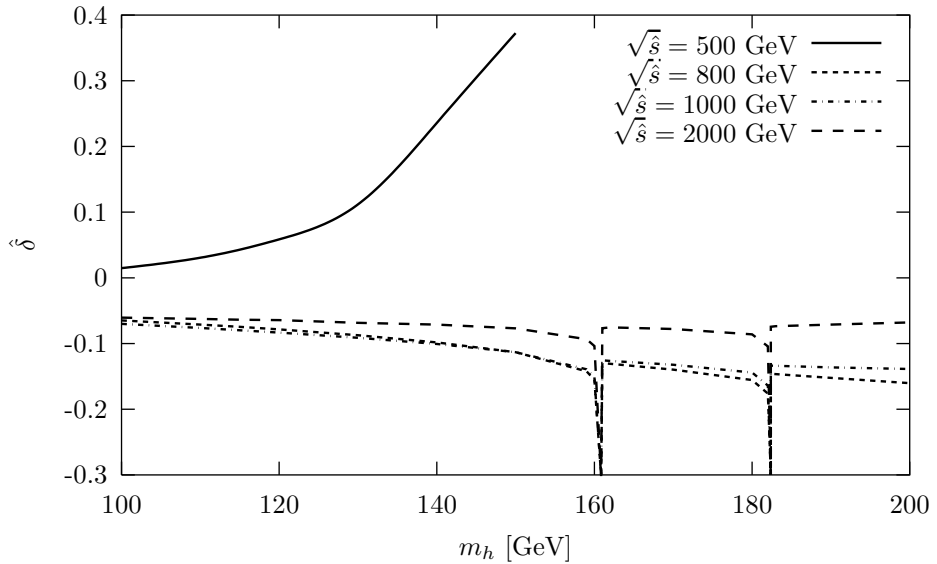


Figure 9: The electroweak relative corrections to the cross sections of $\gamma\gamma \rightarrow t\bar{t}h^0$ subprocess as the functions of the mass of Higgs boson (m_h) with $\sqrt{\hat{s}} = 500, 800, 1000, 2000$ GeV, respectively.

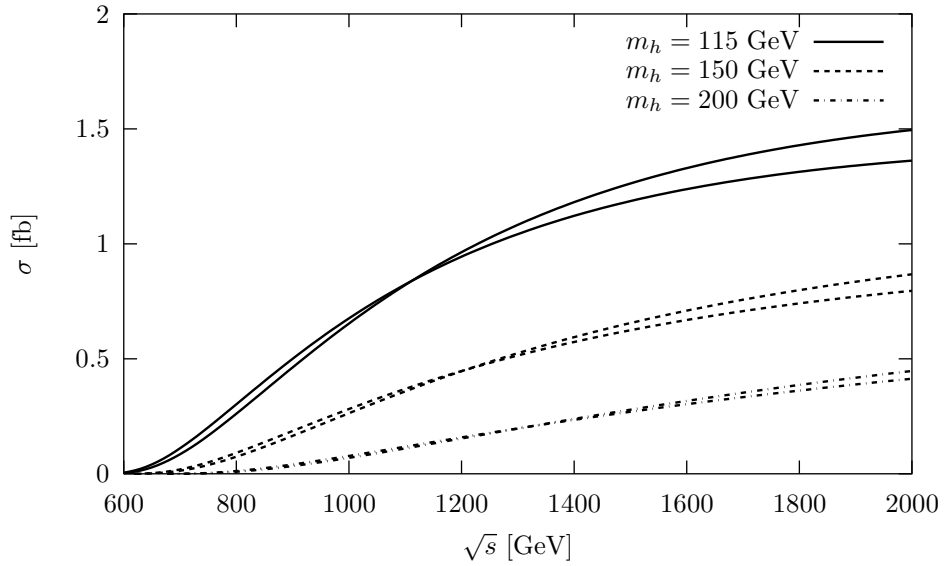


Figure 10: The Born and one-loop QCD corrected cross sections for the $e^+e^- \rightarrow \gamma\gamma \rightarrow t\bar{t}h^0$ process as the functions of c.m.s. energy (\sqrt{s}) with $m_h = 115, 150, 200$ GeV, respectively. For each line type, the upper curve(in the energy region $\sqrt{s} > 1.4$ TeV) is for the Born cross section and the lower one presents the one-loop corrected cross section.

m_h (GeV)	\sqrt{s} (GeV)	$ \delta _{max}$ (%)
115	2000	7.10
130	1700	8.28
150	1435	10.7
170	1220	13.4
200	1020	15.9

Table 2: The maximum absolute relative corrections and the corresponding colliding energy \sqrt{s} positions for the $e^+e^- \rightarrow \gamma\gamma \rightarrow t\bar{t}h^0$ process with $m_h = 115, 130, 150, 170, 200$ GeV, respectively.

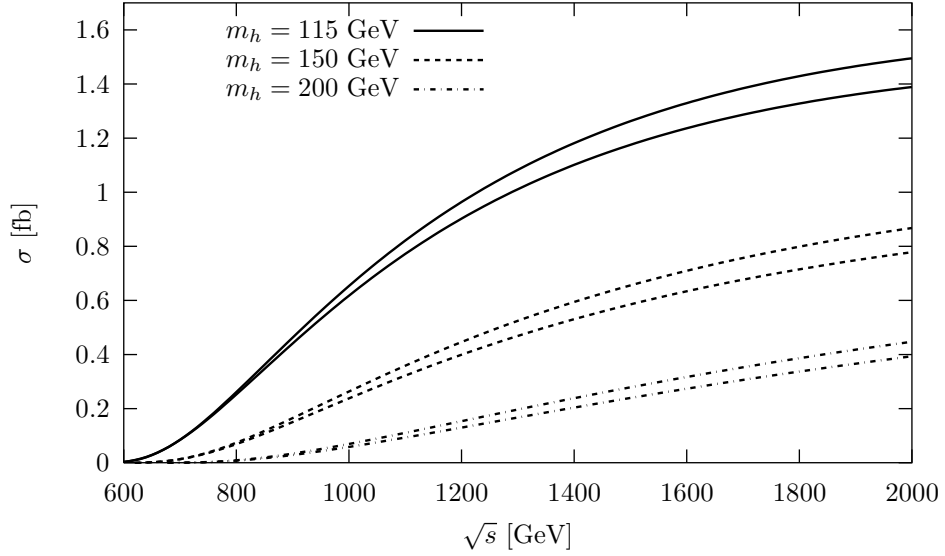


Figure 11: The Born and one-loop electroweak corrected cross sections for the $e^+e^- \rightarrow \gamma\gamma \rightarrow t\bar{t}h^0$ process as the functions of c.m.s. energy (\sqrt{s}) with $m_h = 115, 150, 200$ GeV, respectively. For each line type, the upper curve is for the Born cross section and the lower one presents the one-loop corrected cross section.

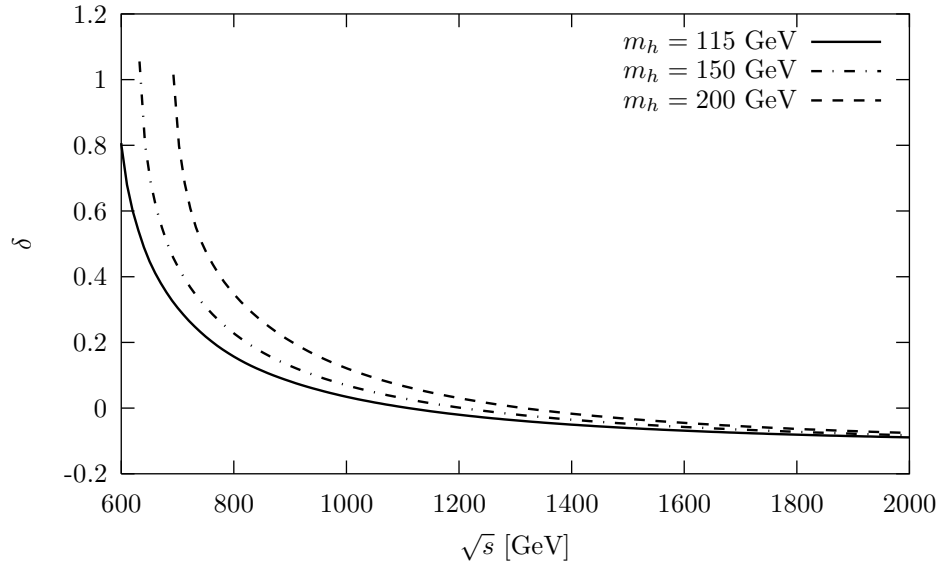


Figure 12: The QCD relative corrections to the $e^+e^- \rightarrow \gamma\gamma \rightarrow t\bar{t}h^0$ process as the functions of c.m.s. energy (\sqrt{s}) with $m_h = 115, 150, 200$ GeV, respectively.

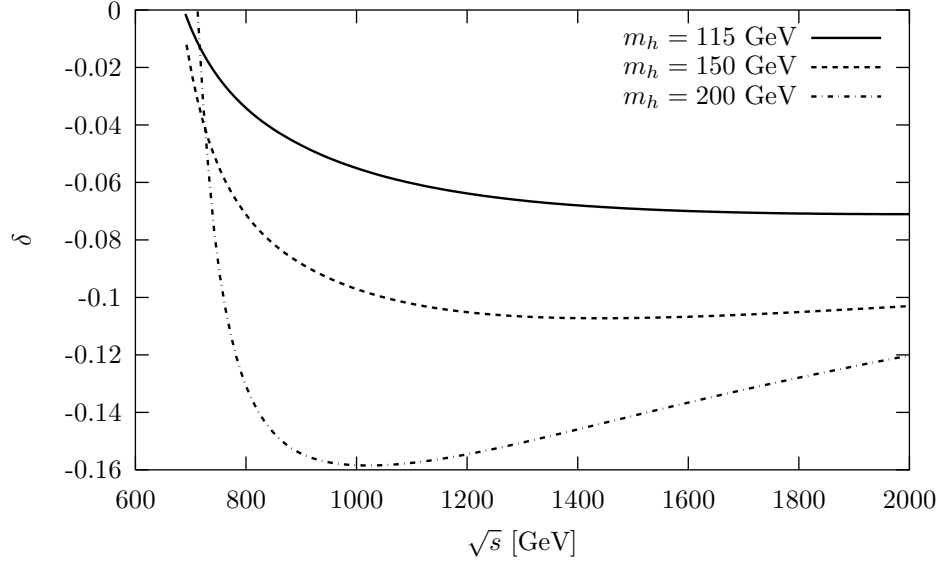


Figure 13: The electroweak relative corrections to the $e^+e^- \rightarrow \gamma\gamma \rightarrow t\bar{t}h^0$ process as the functions of c.m.s. energy (\sqrt{s}) with $m_h = 115, 150, 200$ GeV, respectively.

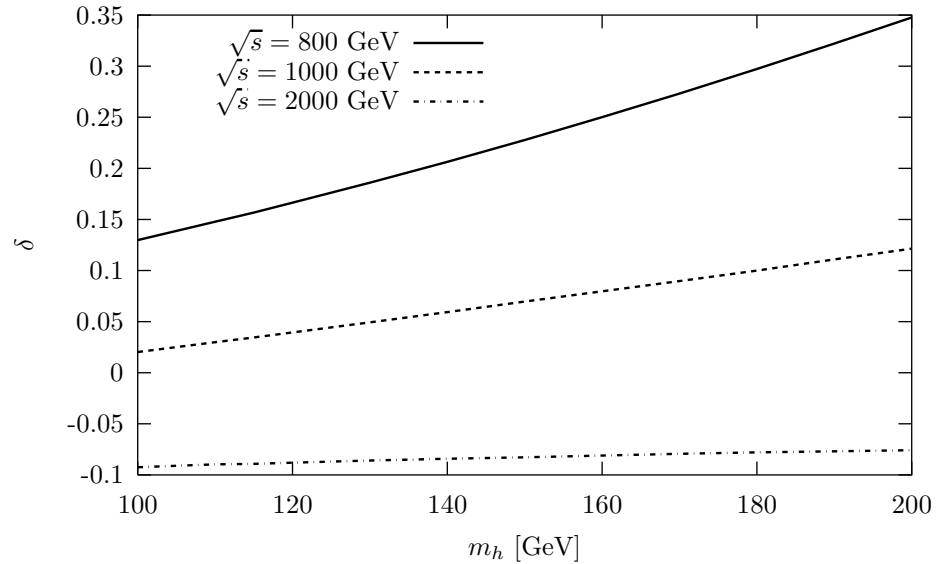


Figure 14: The QCD relative corrections to the $e^+e^- \rightarrow \gamma\gamma \rightarrow t\bar{t}h^0$ process as the functions of Higgs-boson mass (m_h) with $\sqrt{s} = 800, 1000, 2000$ GeV, respectively.

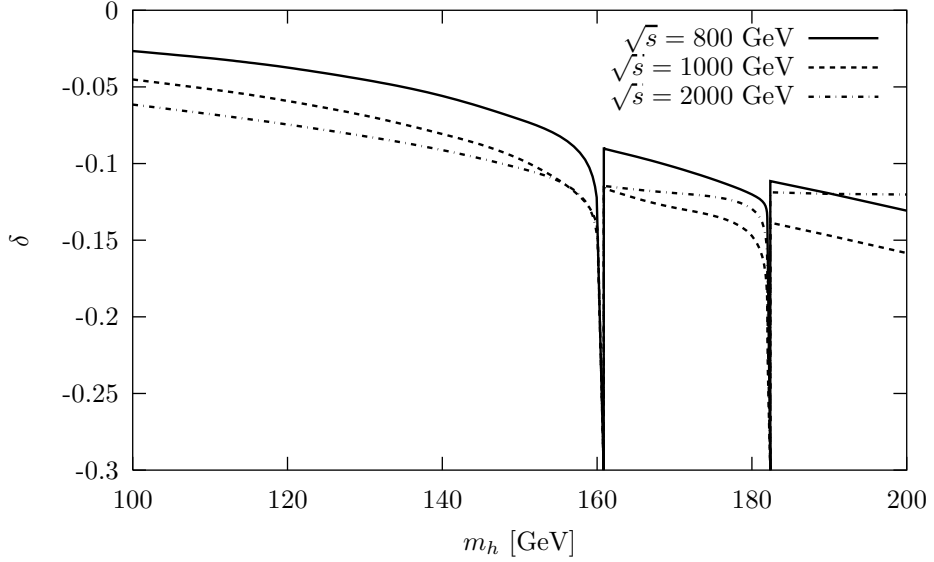


Figure 15: The electroweak relative corrections to the $e^+e^- \rightarrow \gamma\gamma \rightarrow t\bar{t}h^0$ process as the functions of Higgs-boson mass (m_h) with $\sqrt{s} = 800, 1000, 2000$ GeV, respectively.

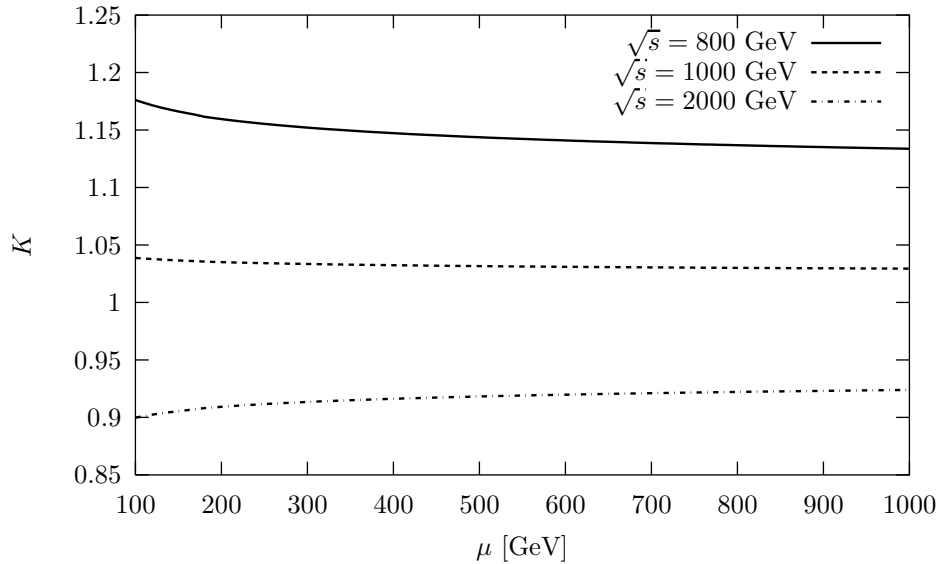


Figure 16: The QCD relative corrections to the $e^+e^- \rightarrow \gamma\gamma \rightarrow t\bar{t}h^0$ process as the function of the QCD renormalization scale μ with $m_h = 115$ GeV and $\sqrt{s} = 800, 1000, 2000$ GeV.

m_t [GeV]	m_h [GeV]	\sqrt{s} [GeV]	σ [fb] (Ref.[20])	σ [fb] (FeynArts)	σ [fb] (CompHEP)
120	60	500	0.45	0.391(0)	0.391(8)
		1000	2.6	2.18(7)	2.19(1)
		2000	2.8	2.39(1)	2.39(1)
150	60	1000	3.2	2.74(1)	2.74(5)
		2000	4.1	3.42(1)	3.42(2)
	140	1000	0.36	0.311(8)	0.311(6)
		2000	0.95	0.805(9)	0.805(6)
180	140	1000	0.40	0.341(3)	0.341(5)
		2000	1.2	1.05(5)	1.05(5)

Table 3: The numerical comparison of the cross sections of the process $e^+e^- \rightarrow \gamma\gamma \rightarrow t\bar{t}h^0$ at tree-level with the results in Ref.[20] by using FeynArts 3 and CompHEP packages.